Diffusion-based microstructure models in brain tumours: Fitting in presence of a model-microstructure mismatch

Umberto Villani [a,b], Erica Silvestri [a,b], Marco Castellaro [a,b], Simona Schiavi [c], Mariagiulia Anglani [d], Silvia Facchini [a,e], Elena Monai [a,e], Domenico D'Avella [a,e], Alessandro Della Puppa [f], Diego Cecchin [g], Maurizio Corbetta [a,e,h], Alessandra Bertoldo [a,b,*]

[a] Padova Neuroscience Center, University of Padova, Padova, Italy
[b] Department of Information Engineering, University of Padova, Padova, Italy
[c] Department of Computer Science, University of Verona, Italy
[d] Neuroradiology Unit, University of Padova, Padova, Italy
[e] Department of Neuroscience, University of Padova, Padova, Italy
[f] Neurosurgery Unit, University Hospital, Padova, Italy
[g] Department of Medicine, Unit of Nuclear Medicine, University of Padova, Padova, Italy
[h] Venetian Institute of Molecular Medicine

A B S T R A C T

Diffusion-based biophysical models have been used in several recent works to study the microenvironment of brain tumours. While the pathophysiological interpretation of the parameters of these models remains unclear, their use as signal representations may yield useful biomarkers for monitoring the treatment and the progression of this complex and heterogeneous disease. Up to now, however, no study was devoted to assessing the mathematical stability of these approaches in cancerous brain regions. To this end, we analyzed in 11 brain tumour patients the fitting results of two microstructure models (Neurite Orientation Dispersion and Density Imaging and the Spherical Mean Technique) and of a signal representation (Diffusion Kurtosis Imaging) to compare the reliability of their parameter estimates in the healthy brain and in the tumoral lesion. The framework of our between-tissue analysis included the computation of 1) the residual sum of squares as a goodness-of-fit measure 2) the standard deviation of the models' derived metrics and 3) models' sensitivity functions to analyze the suitability of the employed protocol for parameter estimation in the different microenvironments. Our results revealed no issues concerning the fitting of the models in the tumoral lesion, with similar goodness of fit and parameter precisions occurring in normal appearing and pathological tissues. Lastly, with the aim of highlight possible biomarkers, in our analysis we briefly discuss the correlation between the metrics of the three techniques, identifying groups of indices which are significantly collinear in all tissues and thus provide no additional information when jointly used in data-driven analyses.

1. Introduction

Since its introduction as a tool of outstanding sensitivity to detect early cerebral ischemic changes in acute stroke patients (van Everdingen et al., 1998), diffusion magnetic resonance imaging (dMRI) has proven its invaluable usefulness in probing tissues' microstructure. Notoriously, the involvement of invasive techniques such as biopsy and subsequent pathological studies are required to retrieve detailed information concerning the anatomy of the brain. With the advent of dMRI, some of these important features became non-invasively accessible. In this field, Diffusion Tensor Imaging (Basser et al., 1994) (DTI) stands out as the most prominent and widely known approach to measure the anisotropic nature of water motion inside biological tissues, both in vivo and *ex vivo*.

Although sensitive to microstructural variations, DTI metrics suffer from poor specificity, as they may be affected by both neurite density and geometrical alterations (Tournier et al., 2011). To overcome this issue, the joint use of high angular resolution diffusion and the multi-compartment modelling of the dMRI signal gave birth to techniques

labelled as 'microstructure imaging' (Alexander et al., 2019), whose aim is that of virtual histology. These models hypothesize that the voxel-wise diffusion signal arises from the composition of several microenvironment of the brain (e.g., cerebrospinal fluid, intra/extra axonal spaces) and try to recover their relative contributions to it in a data-driven fashion.

Although it is possible to fit microstructure models to detect structural changes caused by different pathologies, whenever the normal appearing tissues are disrupted, the generalized use of these techniques requires some additional cares. Such is the case of brain tumours.

In this context, several hypotheses of white matter microstructure models, concerning cell shapes and water diffusivities, no longer hold. This divergence between the biophysical model and the underlying microarchitectural truth causes the impossibility to have a clear physiological interpretation of the diffusion signal (Wen et al., 2015).

Despite the presence of these issues, current state-of-the-art literature is no stranger to the employment of these techniques in gliomas, with a major focus on the use of the Neurite Orientation Dispersion and Density Imaging (Zhang et al., 2012) (NODDI) model. Listing some examples, Masjoodi et al. (Masjoodi et al., 2018) found good separation between oedema, tumour, and normal-appearing tissues; Maximov et al. (Maximov et al., 2017) and Li et al. (Li et al., 2019) showed significant differentiation between different glioma grades, while Kadota et al. (Kadota et al., 2020) reported good discrimination between gliomas and solitary brain metastases. Additionally, Caverzasi et al. (Caverzasi et al., 2016) proposed colour encoded maps of NODDI volumetric fractions which enable fine visual characterization of neoplastic pathologies.

Successful applications like these open the interesting question whether a *microstructure model* (a mathematical expression which gives specific biophysical meaning to its parameter estimates) outside of its physiological assumptions may be used as a *signal representation* (an approximate mathematical description of the data, not based on any theory on the composition of the system it describes) (Novikov et al., 2018). For example, the entire scientific field of radiomics (van Timmeren et al., 2020) relies on the data-driven analysis of texture features, whose link to specific physio-pathological properties is questionable. Radiomics-based models succeed in explaining tumour phenotypes, giving precious information to decision-support techniques for personized treatment (Aerts et al., 2014). With the increasing use of machine learning techniques in the dMRI field (Ravi et al., 2019), parameter maps coming from NODDI or similar alternatives may prove as useful biomarkers to use in conjunction with other imaging modalities to support tumour classification and disease progression monitoring. The current state of the art literature, however, lacks a thorough examination whether proper parameter estimation of these techniques is feasible in tumoral tissues. Indeed, without this assessment, no further consideration regarding the value a parameter may have in this different environment can be made.

Given these premises, in this work we deal with this question. We here aim to investigate whether diffusion-based microstructure models can be properly identified in an environment far from that of their conception. Without making any inference about the physiological meaning and specificity of these techniques in tumours, the assessment we propose here focused on two specific topics: 1) Are there significant model biases in fitting these techniques in the tumoral lesion? 2) Is the accuracy of the parameter estimates completely disrupted by the physiological implausibility of the employed diffusion model?

We tackle these questions by fitting two microstructure models from the literature on a cohort of 11 brain tumour patients and comparing their performance both in the normal-appearing brain and in the tumoral lesion. We are not interested here in comparing performance *between models*, but *between tissues* using the same technique. In particular, because of the growing number of studies using NODDI and the possibility of estimating the compartmental diffusivities (which are not estimated in NODDI) with the direction-averaged approach proposed by the Spherical Mean Technique (Kaden et al., 2016; Kaden et al., 2016)

(SMT), we focus on these two mathematical structures. Additionally, we include in our analysis the Diffusion Kurtosis Imaging (DKI) signal representation (Steven et al., 2014). Due to not making any hypothesis on the underlying microstructure geometry, DKI does not suffer from any model-microstructure mismatch and may be used as reference for intra-model comparison of quality of fit measures in different tissues (Novikov et al., 2018).

We here performed an analysis of model fitting results using the following statistical tools:

- **The Model's Residual Sum of Squares (RSS):** The RSS was computed to evaluate the average goodness of fit for all tissues.
- **The Uncertainty of parameter estimates:** standard deviations of parameter estimates were computed as their Cramer-Rao Lower bound (CRLB) and statistical bootstrapping of the model.
- **The generalized sensitivity functions (GSFs):** in this work, GSFs were introduced to investigate the sensitivity of parameter estimates to the employed diffusion protocols. In other words, can a single diffusion protocol yield reliable parameter estimates in both normal appearing and pathological tissues? We look for an answer to this question using this tool.

The rest of the manuscript is organized as follows: in the "Methods" section, the investigated models/signal representations are briefly introduced, along with the dMRI acquisition details and the framework we use to evaluate model performance; in the "Results" section we report the outcomes separately for each analysis and, lastly, the "Discussion and Conclusion" section provides contextualization of our findings. Here, we highlight the contribution of this work to the literature and discuss its limitations.

2. Methods

The first part of this section gives a brief overview of the models used in this work. As a second point, we explain the metrics we use to evaluate their performance.

A. Models and Signal Representations

The two techniques we fitted to oncological data were the original NODDI implementation and the bi-compartment SMT. These models, while providing different physiological information, share modest protocol requirements in terms of gradient performance. Indeed, one hundred diffusion directions distributed following the static repulsion of charges, taken across two b-shells, are not only sufficient, but also reported as optimal (Zhang et al., 2012). Whole brain quantification is relatively fast, taking 4 h for NODDI (an acceleration down to 5/10 min is possible by employing the AMICO framework (Daducci et al., 2015) and 5 min for the SMT on standard machines. Moreover, by employing solely tensor-like components for the construction of their compartments, they allow the use of the b-value quantity to define the overall diffusion weighting, thus bypassing the need for the separate introduction of its 'microparameters' such as gradient strength and diffusion time. These qualities mark the reason why they are preferentially selected by clinical studies investigating brain microstructure. The DKI technique can be fitted on a similar protocol to the one described above, as the higher b-shell (provided it has b > 1500 s/mm^2) disentangles the non-Gaussian effects of water diffusion in the brain.

1) NODDI

Arguably the most widely known diffusion-based microstructure model, NODDI, adopts a three-compartment formulation aimed to describe the overall signal as a composition of diffusive behaviours in three different environments. As such, the general equation of the model has the following form:

$$A = (1 - V_{iso})(V_{ic}A_{ic} + (1 - V_{ic})A_{ec}) + V_{iso}A_{iso} \qquad (1)$$

where V_{iso} is the isotropic volume fraction and V_{ic} is the intracellular volume fraction. Representing the three model compartments, A_{ic}, A_{iso}

and A_{ec} respectively model the intracellular space by using Watson distributed sticks, the extracellular space with an anisotropic tensor and the free water content with a perfectly isotropic tensor. For a detailed explanation of each compartment, the reader is referred to the original article (Zhang et al., 2012). Accounting for NODDI in its entirety, the complete set of model parameters to be estimated are:

1. V_{ic} [unitless], the intracellular volume fraction.
2. κ [unitless], concentration parameter of Watson distribution.
3. V_{iso} [unitless], the isotropic volume fraction.
4. θ [rad], first Euler angle to describe the mean orientation of Watson distribution in spherical coordinates.
5. φ [rad], second Euler angle to describe the mean orientation of Watson distribution in spherical coordinates.

Technically, κ is the model parameter, the original authors propose to visualize and evaluate the so-called Orientation Dispersion Index, which ranges between 0 and 1 and, (unlike κ), maps higher axonal dispersion into higher values. The fitting routine for NODDI determines the maximum likelihood of parameter estimates with the assumption of additive Rician noise in two steps. Firstly, a brute force search is performed over a coarse and regular grid of possible parameter combinations to provide a preliminary, rough estimate. As nonlinear estimators can be highly sensitive to the initial choice of the parameters, this preliminary step offers reasonable initialization conditions. Consequently, results from the previous phase are carried over to be used as a starting point for the non-linear optimization procedure involving the Gauss-Newton technique. In both steps, the cost function to minimize is the same, and it is the following (Alexander, 2008):

$$L_{ric} = \sum_{n=1}^{M} \left(log(S_n(b,\boldsymbol{G})) - 2log(\sigma) + logI_0\left(D_n\right) - A_n \right) \tag{2}$$

where D_n and A_n are respectively defined as

$$D_n = \frac{S_n(b,\boldsymbol{G})\widehat{S}_n(b,\boldsymbol{G})}{\sigma^2} \tag{3}$$

$$A_n = \frac{S_n(b,\boldsymbol{G})^2 + \widehat{S}_n(b,\boldsymbol{G})^2}{2\sigma^2} \tag{4}$$

With σ being the standard deviation of the Gaussian distribution underlying the Rician distribution, S_n the n-th measurement, $\widehat{S}_n$ the n-th model prediction, b the b-value, $\boldsymbol{G}$ the diffusion gradient direction, M the total number of acquired q-space points and I_0 the Bessel function of the first kind. During the optimization, the volumetric fractions are constrained to belong to the [0 1] interval, while the free water diffusion coefficient and the intrinsic free diffusivity are respectively fixed to $d_{iso} = 3 \cdot 10^{-3}$ mm^2/s and $d_{||} = 1.7 \cdot 10^{-3}$ mm^2/s.

2) SMT

The Spherical Mean Technique model exploit the powder averaging (Callaghan et al., 1979; Kroenke et al., 2004) of the angularly varying diffusion MR signal to obtain a measurement which is independent from the orientation distribution function (ODF) of fibers. As such, SMT does not explicitly model the diffusion signal but rather its b-value dependent mean. Following this rationale, Kaden and colleagues (Kaden et al., 2016) proposed a bi-compartment model, separating intracellular and extracellular environments, which yields the following equations when projected onto its spherical mean:

$$\bar{e}_b = v_{int}\bar{e}_b^{int} + (1 - v_{int})\bar{e}_b^{ext} \tag{5}$$

where v_{int} is the intracellular volume fraction and the two compartments have the following formulations:

$$\bar{e}_b^{int} = \frac{\sqrt{\pi}erf\left(\sqrt{b\lambda_{||}}\right)}{2\sqrt{b\lambda_{||}}} \tag{6}$$

$$\bar{e}_b^{iext} = exp(-b\lambda_{ext})\frac{\sqrt{\pi}\mathrm{erf}\left(\sqrt{b[\lambda_{||} - \lambda_{ext}]}\right)}{2\sqrt{b[\lambda_{||} - \lambda_{ext}]}} \tag{7}$$

where erf is the error function, $\lambda_{||}$ is the intrinsic diffusivity and λ_{ext} follows the tortuosity model $\lambda_{ext} = (1 - v_{int})\lambda_{||}$ (Stanisz et al., 1997). As a difference from NODDI, no compartment is devoted to account for cerebrospinal fluid presence, and diffusivity values are central in the estimation process instead of being fixed quantities. In this case, the complete set of parameters to be estimated is:

1. v_{int}, the intracellular volume fraction.
2. $\lambda_{||}$, intrinsic diffusivity inside the axons.

Another remarkable difference from the NODDI is the choice of the estimator: the SMT bi-compartment model employs a constrained unweighted nonlinear least square approach with the following cost function:

$$C = \sum_{i=1}^{N} \left(\bar{e}_{b_i} - \widehat{e}_{b_i}(v_{int}, \lambda_{||})\right)^2 \tag{8}$$

where N is the number of spherical mean images, $\bar{e}_{b_i}$ is the spherical mean of the diffusion signal taken at the i-th shell and $\widehat{e}_{b_i}$ the prediction of the SMT bi-compartment model. (8) is subject to the constraints $v_{int} \in [0\,1]$ and $0 < \lambda_{||} < \lambda_{free}$ takes place to ensure both diffusivities lie in a physically meaningful range. Constituting the upper bound, λ_{free} is the bulk diffusivity and it is around 3.05 μm^2/ms at 37 °C.

3) DKI

The DKI is an extension of the DTI model which adds a quadratic term in the b-value series expansion of the dMRI signal to quantify the degree of non-Gaussian diffusion occuring inside the different tissues. Like DTI, DKI does not make any physiological assumptions about possible diffusion behaviours inside/outside cellular object and is therefore referred to a signal representation. The formula for the DKI is given by the second-order approximation of the Taylor expansion of the noiseless diffusion-weighted signal around b = 0:

$$\ln[S(\boldsymbol{b},\mathbf{g})] = \ln[S(0)] - b\sum_{i,j=1}^{3} g_ig_jD_{ij} + \frac{b^2}{6}\left(\sum_{i=1}^{3}\frac{D_{ii}}{3}\right)^2\sum_{i,j,k,l=1}^{3} g_ig_jg_kg_lW_{ijkl} \tag{9}$$

where S is the diffusion signal, g_i are the diffusion gradient directions, D_{ij} are the components of the diffusion tensor and W_{ijkl} are the components of the diffusion kurtosis tensor. As the fitting of the DKI model can be formulated as a linear regression problem, we used the readily available MATLAB toolbox implementing the weighted linear least-square estimator (Veraart et al., 2013) described by the equation

$$\boldsymbol{p} = (\boldsymbol{X}^T\boldsymbol{W}\boldsymbol{X})^{-1}\boldsymbol{X}\boldsymbol{W}\boldsymbol{y} \tag{10}$$

Where $\boldsymbol{p}$ is vector containing the parameters of the model, $\boldsymbol{X}$ is the design matrix of the regression problem, $\boldsymbol{y}$ is the vector of the observed diffusion signal, and $\boldsymbol{W}$ is the diagonal weight matrix containing the square of the observed signal.

D. Assessment Metrics

1) Residual analysis

One of the most practical ways to assess whether a model can accurately represent the diffusion signal is to look at the behaviour of its residuals, which are defined as:

$$r(b_i, \boldsymbol{G}_i) = S(b_i, \boldsymbol{G}_i) - \widehat{S}(b_i, \boldsymbol{G}_i) \tag{11}$$

where S is the measured signal, $\widehat{S}$ is the model prediction, b_i is the b-value and $\boldsymbol{G}_i$ is the diffusion gradient direction. To explain their usefulness, let the diffusion signal be represented as:

$$S(b_i, \boldsymbol{G}_i) = S_{true}(b_i, \boldsymbol{G}_i) + n(b_i, \boldsymbol{G}_i) \tag{12}$$

where S_{true} is the physiological source of the signal and n is the additive noise. Under the hypothesis that the used microstructure model is

a good approximation of the noiseless source (i.e., $\widehat{S} \cong S_{true}$), the model residuals are an estimation of a random realization of n:

$$r(b_i, \boldsymbol{G}_i) = n(b_i, \boldsymbol{G}_i) \tag{13}$$

From (11), essentially, we assess whether model residuals are centred around zero and whether their variances are comparable to that of the additive noise. Such a qualitative analysis, valid in the case of Gaussian noise, is extended to the Rician case, as for SNR > 2 the two probability distributions have similar properties (Gudbjartsson and Patz, 1995). When looking at magnetic resonance (MR) images composed by several hundred thousand voxels, the inspection of all generated residuals can be substituted to the computation of the Residual Sum of Squares (RSS), to recover a voxel-wise scalar measure of model fit quality. The RSS is mathematically defined as:

$$RSS = \sum_{i=1}^{N} r(b_i, \boldsymbol{G}_i) \tag{14}$$

where N is the number of the acquired q-space points. Under the hypothesis noise is invariant to the gradient direction and b-value changes, one can also derive a voxel-wise estimation of the standard deviation σ of the measurement. For each voxel, this was done by approximating σ as the standard deviation computed across the multiple b0 measurements (Tournier et al., 2011). Subsequently, we computed the expected RSS (i.e, the RSS a model should approximately have if it is in accordance with the underlying noise hypotheses) as:

$$E[RSS] = \sigma^2 N \tag{15}$$

2) Uncertainty of estimated microstructure parameters

To assess whether the estimation process of the given model yields robust and reproducible results in vivo, it is necessary to understand how the intrinsic variance of the measurement error affects the final parameter estimate. One way to tackle these problems relies on the use of statistical bootstrapping (Kappy, 2013) to extract variability from the dataset. Statistical bootstrapping in the modelling context can be summarized by the following steps:

1. Fit the MR signal with the employed diffusion model and compute the model prediction and residuals.
2. Obtain a unique permutation of the extracted residuals and add it the model prediction
3. Fit the newly synthetized diffusion signal with the model again, obtaining a new vector of parameter estimates
4. Given all the iterations, compute the standard deviation of parameter estimates.

This technique requires extensive computational power, as multiple model fitting steps are required to achieve statistical significance.

A second, less time-demanding, strategy can be pursued by exploiting a theoretical result from the mathematical statistics frame known as the Cramer-Rao Lower Bound (CRLB). Briefly, let the Fisher information matrix be:

$$J_{i,j} = E\left[\frac{\partial^2 L}{\partial w_i \partial w_j}\right] \tag{16}$$

where L is the log likelihood of the measurement with the appropriate noise model and $w_{i,j}$ are the model parameters. If the partial derivatives $\partial L/\partial w_i$ exist, the used estimator is unbiased and matrix J is invertible, then

$$\Sigma_p \geqslant J^{-1} \tag{17}$$

where Σ_p is the covariance matrix of the parameter estimates. Equation (17) effectively means, for the single model parameters that:

$$\sigma^2 \geq (J^{-1})_{i,j} \tag{18}$$

The Fisher information matrix J has a closed form solution when the additive noise model is Gaussian. However, when this assumption becomes Rician, which is valid in general for MR magnitude images (Gudbjartsson and Patz, 1995), the formulation becomes less trivial and, borrowing the results from (Alexander, 2008), the information matrix becomes:

$$J_{i,j} = \sum_{k=1}^{K} \frac{1}{\sigma^4} \frac{\partial \widehat{S}}{\partial w_i} \frac{\partial \widehat{S}}{\partial w_j} \left(Z_k - \widehat{S}_k^2\right) \tag{19}$$

where K is the number of measurements and Z_k has the following form:

$$Z_k = \int_0^\infty \widehat{S}_k^2 I_1^2\left(\frac{\widehat{S}_k S}{\sigma^2}\right) I_0^2\left(\frac{\widehat{S}_k S}{\sigma^2}\right) P_{ric}(S) dS \tag{20}$$

where $I_{0,1,\ldots,n}$ are the modified Bessel functions of the first kind and P_{ric} denotes the Rician distribution. As presented in the original article (Alexander, 2008), the integral in (20) requires numerical approximation and computing its exact values for Z_k is computationally intensive. Thus, we precompute a grid of possible fixed values and we rely on linear interpolation to recover pointwise estimates.

The evaluation of CRLB derived variance metrics and the model residuals are common practice in modelling in medicine and as such they mark the basis of the analysis in this article.

3) Sensitivity analysis of the model equation

Sensitivity equations are often used in simulation studies of physiological systems to understand how a variation of model parameters affect model outputs (Frank and Eslami, 1980). They are generally used for optimal experiment design purposes, but we here used them to the test whether the employed protocol was suitable for parameter estimation in all different tissues.

More specifically, we adopted the GSFs formulation proposed by Tomaseth and Cobelli (Thomaseth and Cobelli, 1999). Briefly, GSFs recover, in a context where time is the independent variable, which temporal sub-intervals are informative for a particular model parameter. This is done by evaluating the Fisher Information conveyed on a model parameter by a hypothetical observation and normalizing it by the total information provided by the entire set of the evaluated observations. Thus, for each model we compute the Generalized Sensitivity matrix as:

$$\mathbf{GS}(b_J) = \sum_{j=1}^{J} \left[\sum_{m=1}^{M} \mathbf{I}_\theta(b_m)\right]^{-1} \boldsymbol{I}_\theta(b_j) \tag{21}$$

where GS is the Generalized Sensitivity matrix computed on a subset of the b-values b_J, M is the length of the b-value vector $\boldsymbol{b} = [b_1, b_2, \cdots, b_M]$, and $I_\theta(\beta)$ is the Fisher Information matrix computed from observations coming from a diffusion shell at b-value equal to β, according to (16). GSFs for all separated parameters are then extracted as:

$$gsf_\theta(b_J) = diag(\mathbf{GS}(b_J)) \tag{22}$$

Operatively, we evaluate GSFs for both NODDI and the SMT bi-compartment model on increasingly higher diffusion shells in the range b $\in$ [0 4000] s/mm^2 with 30 uniformly distributed gradient directions. Model parameter values for the generation of GSFs of a specific tissue were chosen as their median across that tissue for a representative subject of the dataset.

E. In vivo acquisition

Eleven patients suffering from de novo brain tumours have been scanned at the University Hospital of Padova. All procedures were in accordance with the ethical standards of the institutional research committee and with the 1964 Helsinki declaration plus later amendments. All participants provided informed, written consent in accordance with the local University Hospital Institutional Review Board. The demographical information of the patients' cohort is reported in Supplementary Table 1.

DWIs have been acquired on a Siemens Biograph mMR-PET/MR scanner at 3 T equipped with the PET compatible 16-channels Siemens head and neck coil (TR/TE 5355/104 ms; 2.0x2.0x2.0 mm^3). Each volume was composed of 68 slices, acquired in interleaved mode with a multiband accelerator factor of 2 (CMRR, R014) and no in-plane acceleration. The multi-shell diffusion protocol was composed by a total of 100 diffusion weighted images, subdivided in the following way:

- 10 b0 images, with zero diffusion weighting
- 30 diffusion weighted images at b-value = 710 s/mm^2 (Shell 1)
- 60 diffusion weighted images at b-value = 2855 s/mm^2 (Shell 2)

In varying the b-value, diffusion time and impulse duration have been kept fixed to values $\Delta = 50.05ms$ and $\delta = 27.77ms$, while gradient strength G was altered. This diffusion HARDI protocol is the optimized two shell NODDI protocol as described in (Zhang et al., 2012). Each diffusion volume has been acquired in both Anterior-Posterior (AP) and Posterior-Anterior (PA) phase encoding direction for pre-processing needs, as explained in a subsequent section.

In the same MR session, a reference 3D T2-weighted Fluid Attenuated Inversion Recovery (FLAIR) image (TR/TE 5000/395 ms; 1.0x1.0x1.0 mm^3; FOV 250 mm), two T1w structural images (TR/TE 2400/3.2 ms, 1.0x1.0x1.0 mm^3), FOV 256 mm, 160 slices) acquired both before and after contrast agent injection, and a T2w structural image (TR/TE 3200/536 ms, 1.0x1.0x1.0 mm^3), FOV 256 mm, 160 slices) were acquired.

F. Preprocessing of images

The acquired diffusion weighted volumes were visually inspected to identify and remove those images affected by interslice instabilities (Bastiani et al., 2019) which were deemed excessively corrupted for subsequent pre-processing techniques to correct. The rest of the pre-processing was executed in its entirety within the *MRtrix* Software (MRtrix3, xxxx) and features an initial denoising step based on random matrix theory (Veraart et al., 2016), and a subsequent call to the tools *topup* (Andersson et al., 2003) and *eddy* (Andersson and Sotiropoulos, 2016) from the *FMRIB Software library* (FSL) for B0 inhomogeneity, eddy current and motion joint correction. Tumour masks to separate the tumour core and the oedema from healthy tissue were manually drawn by an expert radiologist on the acquired T1w, T2w and FLAIR images and were subsequently coregistered to the mean b0 volume with the *Advanced Normalization Tools* (ANTs) (Avants et al., 2011) toolbox. The T1w images were segmented into cortical and subcortical grey matter, white matter, and CSF with the *Statistical Parametrical Mapping (SPM12)* toolbox (Ashburner, 2014). Segmentation results were coregistered to the mean b0 volume using ANTs by applying an affine transformation previously estimated on the T1w image.

G. Model Fitting software and Statistical Analysis

We fitted NODDI, SMT and DKI to the acquired oncological dataset using off-the-shelf toolboxes which are publicly available (http://mig.cs.ucl.ac.uk/index.php?n=Tutorial.NODDImatlab for NODDI, https://github.com/ekaden/smt for SMT and https://cai2r.net/resources/software/diffusion-kurtosis-imaging-matlab-toolbox for DKI) and integrated some in-house MATLAB scripts to compute the RSS, the voxel-wise approximation of parameter standard deviation (σ) through the Cramer-Rao inequality (for SMT and NODDI) and statistical bootstrapping (for DKI), and the GSFs for all techniques. Subsequently, by computing the GSFs, we evaluated the general sensitivity of model parameters to investigate whether the different microstructural environments (i.e., WM, GM, tumour core and oedema) affect the optimality of the employed diffusion protocol. Lastly, we briefly discuss the orthogonality of information these diffusion parameters may convey in differentiating physiological differences among the different tissues. Pearson's correlation between voxel-wise parameter values was computed for every subject, and its across-subject median was subsequently extracted. From median tissue-specific matrices, we eventually computed the parameter Redundancy Matrix (RM) by thresholding the
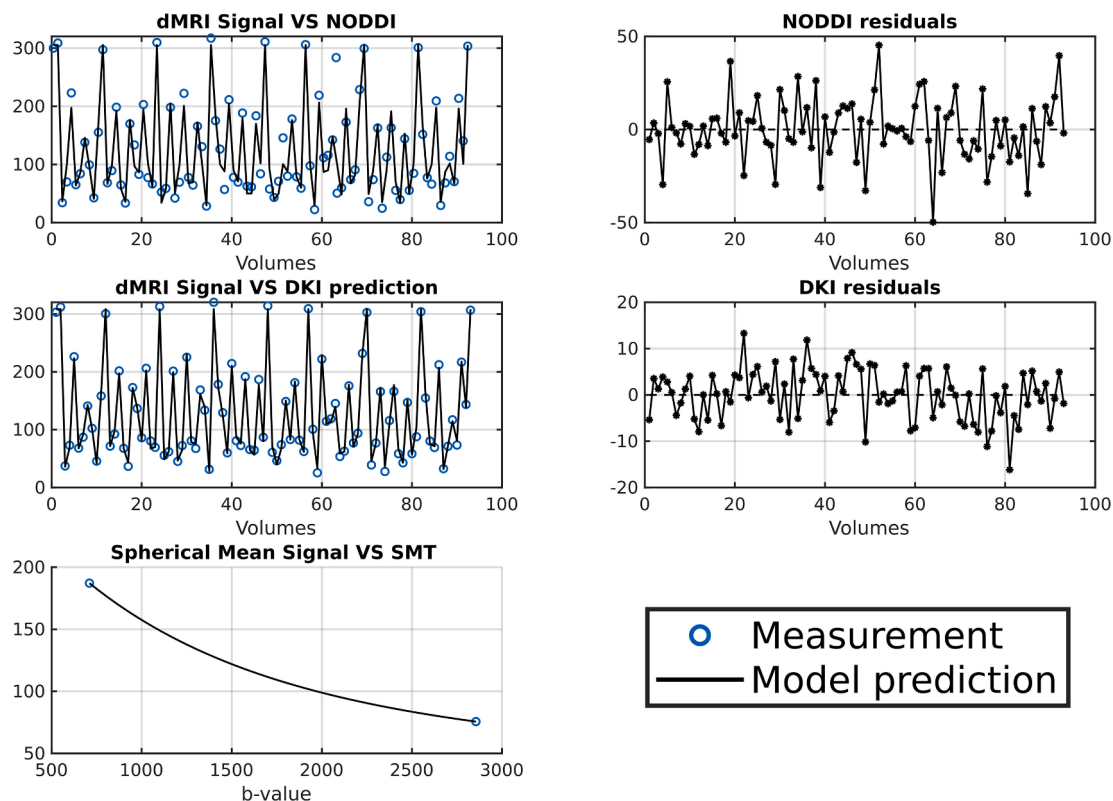

Fig. 1. On the top row, visualization of the diffusion signal along with NODDI model prediction and its residuals. On the mid row, the DKI model prediction of the diffusion signal and its residuals. On the bottom row, the spherical mean of the signal and the SMT bi-compartment model prediction.

four matrices at ρ = 0.5 and computing their intersection. The RM matrix delineates those strong correlations between parameters which are common to all tissues.

3. Results

1) Signal considerations, model fitting and parameter precisions

Fig. 1 shows an example of the voxel-wise model fit for NODDI/SMT/DKI and highlights how the three techniques quantify microstructure information in very different ways. While NODDI and DKI are fitted on the directionally variable diffusion signal, the SMT is a model for its spherical mean, thus reducing the number of independent points to the number of the acquired b-values. This has repercussions in terms of the feasibility of residual analyses of the model in case of two-shells HARDI acquisitions such as the one featured here. As the model has only two degrees of freedom, the fit results in a perfect interpolation of the available data, rendering the computation of residuals trivial and non-informative in terms of goodness-of-fit. In the other two cases, model residuals have definite meaning, and their derived metrics can be reliably quantified. In the representative example in the figure, the average of NODDI and DKI residuals are respectively $\mu_{NODDI} = 0.0748[A.U.]$ and $\mu_{DKI} = 0.127[A.U.]$, denoting the absence of model biases in terms of fitting. Standard deviations for this example fit are $\sigma_{NODDI} = 16.61[A.U.]$ and $\sigma_{DKI} = 5.61[A.U.]$, with σ_{NODDI} higher σ_{DKI}, but both comparable with the estimation of the noise standard deviation through the b0 images $\sigma_{noise} = 6.26[A.U.]$.

Fig. 2 shows both the maps of microstructure parameters of the three diffusion techniques and those of their relative standard deviation for an axial slice of a representative patient. Although the modelling choices for the various compartments may be physiologically questionable in tumours, the employed parameter estimators are able to react to the different features of the diffusion signal and output spatially coherent metrics, both in terms of their value and uncertainty. NODDI and SMT parameter maps appear to have a good degree of spatial continuity in the pathological area, revealing unique contrasts which are not seen in structural images and in the DKI model. The standard deviation images also show a varying degree of spatial smoothness both in normal appearing tissues and in the tumoral lesion. Although standard deviations are very close in numerical values, some slight trends can be observed, where the tumoral lesion appear to have higher precision with respect to normal appearing tissues for all parameters except for NODDI's ODI.

These representative single-slice observations are generalized in Fig. 3, which shows the boxplot of the voxel-wise parameter estimates and their standard deviations for all subjects in the dataset. While the single parameters show heterogeneous patterns between healthy and tumoral tissues and appear to have different discrimination power, their standard deviation does not dramatically differ between the lesion and the normal appearing brain. As shown in the previous figures, slight differences between tissues are still present, with a tendency of σ to be lower for oedema and tumours for most parameters. Overall, the general trend suggests that estimation precision is stable both in healthy and pathological tissues. As this behaviour is common both to DKI and to the two microstructural models, it suggests the model-microstructure-mismatch does not significantly impair parameter estimation precision when fitting NODDI and SMT inside tumoral tissues.
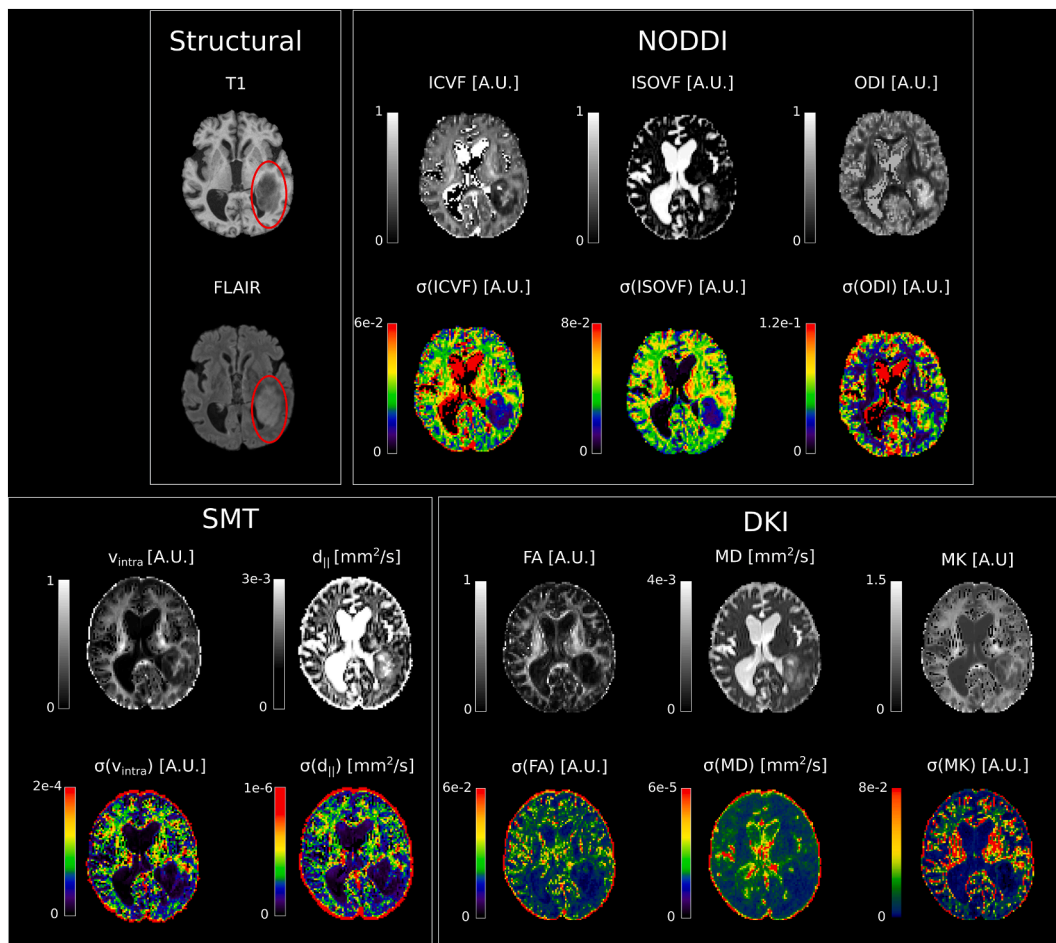

Fig. 2. An example axial slice from a representative patient showing its T1w and FLAIR structural images as well as both NODDI/SMT/DKI metrics (first row of each box, grey scale) along with their standard deviation map (second row, jet scale).
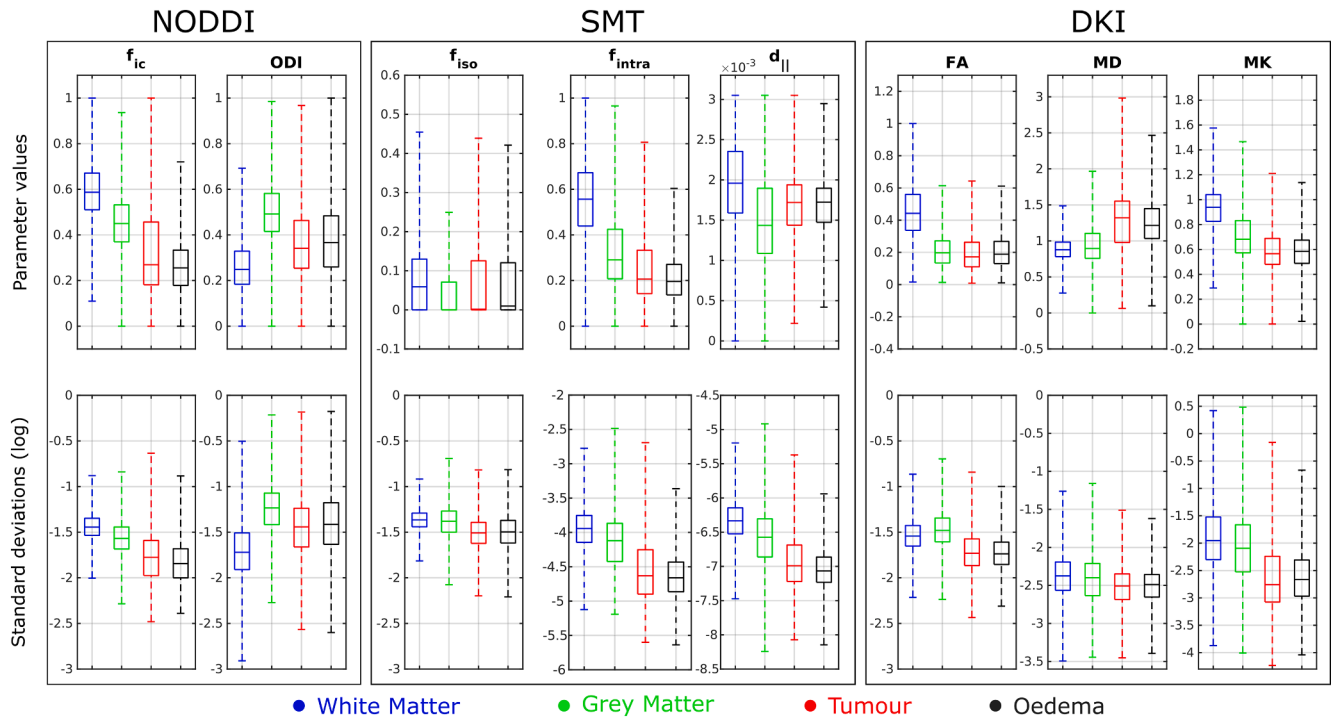
Fig. 3. Boxplots for tissue-specific mean and standard deviations (log10 scale) of NODDI, SMT and DKI metrics coming from normal-appearing white matter in blue, grey matter in green, tumoral tissues in red and from the oedema region in black. (For interpretation of the references to colour in this figure legend, the reader is referred to the web version of this article.)

Table 1 shows both the tissue specific mean RSS across all subjects for NODDI and DKI, and its expected value given the appropriate noise model. As it was observed in the case of parameter precisions, it appears that the residuals from both techniques are not particularly affected by the pathological environment in the tumour and in the oedema. The fitting performance seems unaltered in the general picture, with both techniques being fairly in agreement with the expected RSS given the estimation of the noise. It is worth mentioning that, as the used estimators are different, it is difficult and beyond the scope of this work to draw any conclusions about an inter-model comparison of goodness-of-fit. Moreover, as the residuals of SMT model are uninformative due to the aforementioned reasons, its RSS was not computed.

2) Generalized sensitivity of the models

Fig. 4 shows the GSF plots for the model parameters of NODDI, DKI and SMT, generated as explained in the methods section.

Concerning the behaviour of single diffusion parameters, we can identify three different trends: A first set of parameters (f_{iso}, $d_{||}$ and the diffusion tensor components) gain their informational content in the b-

values approaching $b = 1000$ s/mm^2; a second set of parameters (f_{ic}, f_{intra} and the diffusional kurtosis tensor components) benefit from b-values starting from $b = 2500$ s/mm^2 and a single parameter (Watson's distribution concentration parameter k) steadily gains information across the entire studied b-value range, with no clear optimal interval.

The general behaviour of the curves for every parameter does not significantly vary across the different tissues, identifying 0–1 rises which are relatively similar between normal WM, GM, oedema, and the tumour. Similarly, to what happens for the DKI, the lack of difference in general sensitivity for the two microstructural models suggest a single acquisition protocol features similar estimation precision for all tissues. We believe this finding confirms that fitting these techniques inside the tumoral lesion do not require a modification of the diffusion protocol in use, which was designed specifically for healthy subjects.

As a last remark, significant over/undershoot from the 0–1 range for the GSFs reveals substantial correlations during the estimation process of same-model parameters, which in this case tends to be tissue dependent, as it will be discussed in the following section.

Table 1

Mean residual sum of squares for each subject and tissue in the dataset. The set of columns to the right represents the expectations of the RSS, given the standard deviation of the noise affecting the diffusion signal. Results are reported in logarithmic scale (log10). Cells marked with "x" denote subjects for which no oedematous tissue was found in the lesion segmentation procedure.

| Subj	DKI log(RSS)				NODDI log(RSS)				Expected log(RSS)			
	WM	GM	Tum	Oed	WM	GM	Tum	Oed	WM	GM	Tum	Oed
#01	3.678	3.792	3.718	3.869	4.129	4.037	3.858	4.139	4.063	4.328	4.272	4.411
#02	3.651	3.768	3.764	3.789	4.106	4.079	4.065	4.160	3.886	4.157	4.394	4.098
#03	3.615	3.061	3.769	3.688	4.061	3.987	4.356	4.168	3.887	4.096	4.139	4.044
#04	3.544	3.734	3.496	x	4.035	4.013	3.722	x	3.844	4.204	4.144	x
#05	3.713	3.875	3.775	3.842	4.185	4.104	4.046	4.222	4.043	4.412	4.347	4.515
#06	3.701	3.895	3.634	3.548	4.146	4.097	4.026	3.997	4.027	4.373	3.959	4.092
#07	3.577	3.405	3.632	x	4.096	3.914	4.063	x	3.830	3.985	3.901	x
#08	3.618	3.666	3.646	3.752	4.062	3.974	4.089	4.067	3.978	4.102	4.126	4.389
#09	3.571	3.754	3.649	3.818	4.021	4.010	4.115	4.182	3.914	4.304	4.028	4.523
#10	3.679	2.686	3.762	3.721	4.166	4.062	3.981	4.143	4.052	4.375	4.191	4.199
#11	3.538	3.172	3.752	3.625	4.119	4.020	4.132	4.198	3.753	3.940	4.328	4.057
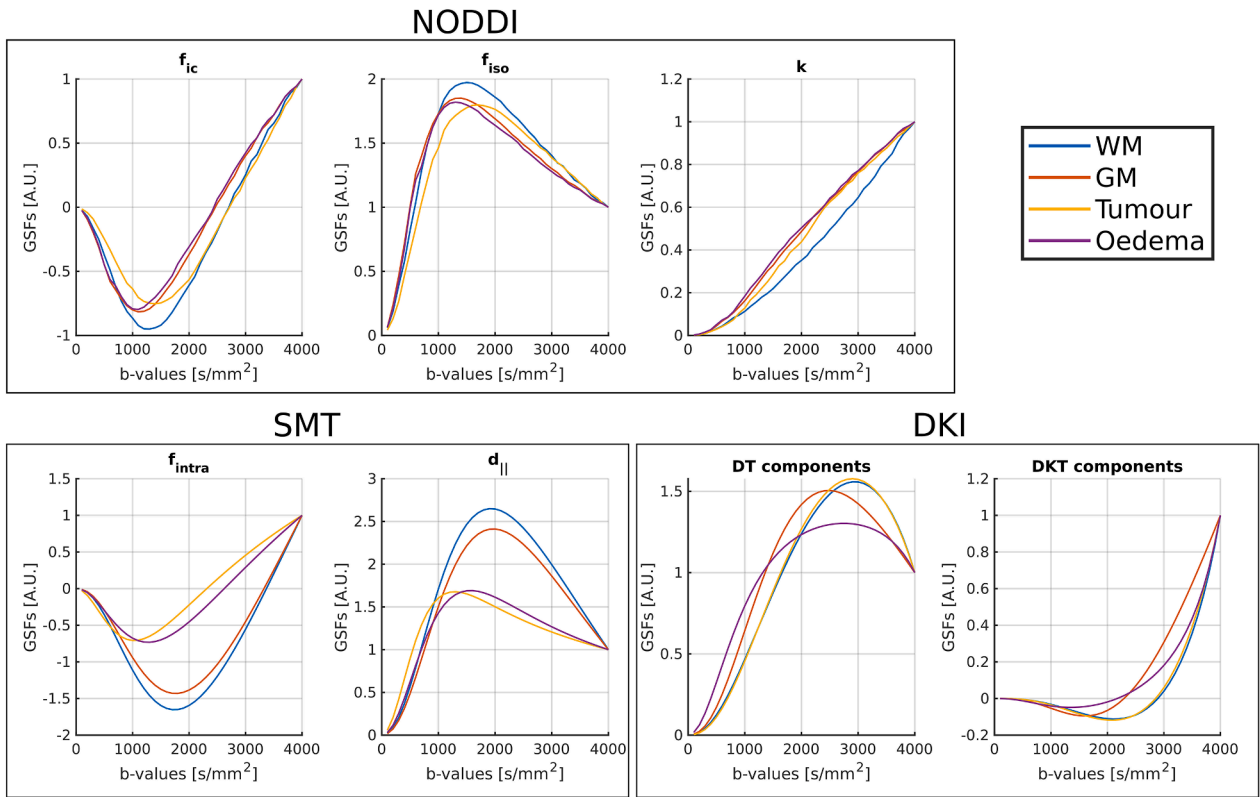
Fig. 4. Generalized sensitivity equations for the NODDI, SMT and DKI generated with parameter values corresponding to voxels from white matter, grey matter and the tumoral tissues (tumour core and oedema). The DKI section contains the mean GSF for the parameters of the kurtosis-corrected diffusion tensor (DT components) and the mean GSFs across the parameters of the kurtosis tensor (DKT components). The interval for which we have the 0–1 transition marks b-value range which is most informative for each of the model parameters.

3) Investigating parameter correlations

Lastly, Fig. 5 (a-d) shows the median correlation matrix across all subjects of the voxel wise parameters from all models, computed for the four studied tissues. These matrices present significantly different structures, supporting the hypothesis that relationships between diffusion parameters change inside pathological voxels. However, we find some strong correlations, both positive and negative, which tend to be present in all the tissues. Fig. 5.e shows the redundancy matrix (RM).
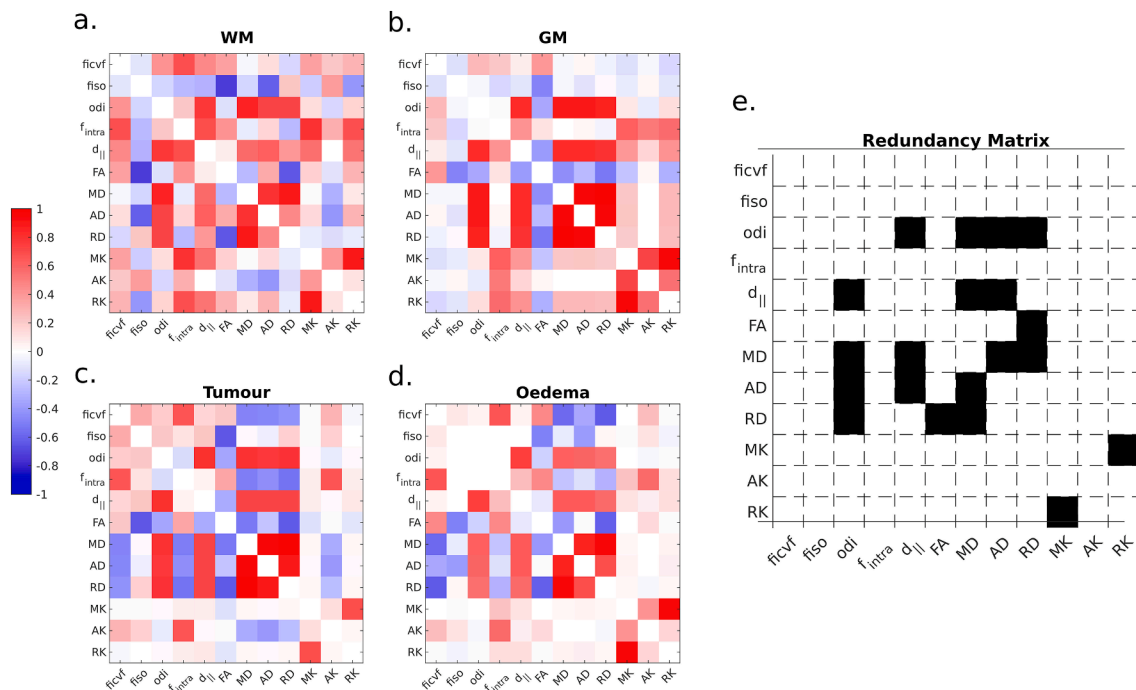

Fig. 5. (a-d) Median voxel-wise correlation matrices for the computed diffusion metrics for all subjects in the dataset; (e) Metrics Redundancy Matrix, highlighting strong parameter correlations common to the structure of matrices a-d. For clarity of view, main diagonal values (trivially equal to 1) were put to 0.

The occurrences in the RM reveal those couples of metrics which feature high correlation (non-orthogonality of information) and are additionally common to all tissue-specific matrices (poor tissue discrimination power). In particular, the AD, MD, and RD diffusivity metrics from DKI, ODI from NODDI and $d_{||}$ from the SMT appear to be strongly related, suggesting the entire inclusion of this subset of diffusion metrics in any data-driven procedure to be redundant. Similar considerations can be made about the MK-RK pair, for which the combined use is discouraged. All relationships highlighted by the RM were statistically significant in all subjects, with pvalues inferior to p = 10e-28.

4. Discussion

In this article, we explore the use of advanced diffusion models in tumours from the standpoint of goodness of fit and precision of their estimates. We refrained from giving explicit biophysical meaning to their parameters due to the microstructure-model mismatch such choice features, and concentrated on investigating their stability in the pathological tissues as signal representations. In doing so, we separately assessed their mathematical reliability in the tumoral lesion and in the normal appearing tissues. We questioned whether we would consistently find worse model residuals and less precise parameter estimates, as we thought the discrepancy between the tumour architecture and the biophysical model formulation would result in the inability to properly identify the model. We noticed, however, how the parameter estimation procedure is minimally impacted by the tissue-model mismatch, resulting for some cases in light trends of higher precision inside the tumoral tissues with respect to the normal-appearing brain. This is most surprising when it comes to the intra-axonal compartments of both NODDI and SMT, where we feel the structural mismatch is most present. Highly anisotropic, 'stick-like', neuronal structures are mostly absent in tumours, yet the corresponding parameters are identified precisely and with a certain degree of spatial coherence. To our knowledge, the use of the stick diffusion model is known in tumour diffusion modelling. In fact, the Vascular, Extracellular, and Restricted Diffusion for Cytometry in Tumours (VERDICT-MRI) model for colorectal and prostate cancer (Panagiotaki et al., 2015; Panagiotaki et al., 2014) employs isotropically dispersed sticks to describe pseudo-diffusion inside blood vessels. Nevertheless, this information comes from diffusion volumes at very low b-values ($<$300 s/mm^2) (similarly to Intravoxel Incoherent Motion (IVIM) MRI (Le Bihan et al., 1986), which are not acquired in typical HARDI datasets such as ours.

It should be noted that, while the methodology used in this work is sound for comparing fitting results of *the same model in healthy and pathological conditions*, it is not appropriate for the comparison of *different models*. Indeed, DKI features consistently lower residuals than NODDI across tissues. However, as different estimators are used for the two techniques, lower RSS does not necessarily indicate that DKI performs better in the tumoral tissue. Moreover, the standard deviation of the measurement noise was estimated from the multiple b0 images acquired, thus disregarding possible contributions from varying b-value and gradient direction. Thus, we cannot establish if DKI is underestimating or NODDI is overestimating the noise level.

It is interesting to notice how the SMT estimation leads to dramatically higher relative precision for the intracellular volume fraction with respect to NODDI (up to 3–4 orders of magnitude smaller values of σ). This observation however does not come completely unexpected, as the spherical mean signal is produced with a significant direction averaging procedure which comes with the benefit of suppressing the additive Gaussian-like noise.

Overall, we found significant evidence that the model-microstructure mismatch does not substantially affect the fitting performance of NODDI and the SMT in the tumoral lesion, as similar trends in the studied metrics are witnessed for the DKI signal representation. The information and novel contrast these parameter maps produce appears to be stable and may potentially be exploited by data driven approaches to analyse different microstructural environments. In this work, we give useful indications about which of the studied metrics provide information about tissues (pathological and healthy) which is non-collinear and investigate ways to discriminate those which are non-informative, in relation to their collective use.

While model identification appears to be optimal, we still advise to use additional caution to give a pathophysiological interpretation to single parameters when applying 'biophysical' models in tumours. Indeed, the comprehension of their mathematical structure, assumptions, and limitations, is vital to make any biological inference. If proper validation in this pathological environment is not provided, NODDI and SMT remain geometrical models of diffusion, or signal representation, not specifically linked to any biological features.

Probing the microstructural environment of brain tumours through diffusion imaging may yield useful biomarkers to monitor progression and treatment response, but there is still room for various improvements (Nilsson et al., 2018). Apart from the use of advanced models, the use of peculiar acquisition schemes may enrich the diffusion signal enough to move past the model identification degeneracies reported in recent literature (Jelescu et al., 2016; Novikov et al., 2019), and more unconventional datasets acquired with multiple diffusion times (Panagiotaki et al., 2015) or 'B-tensor encoding' (Szczepankiewicz et al., 2019) are recent signs that the research framework of dMRI pulse sequence design still has a lot to offer.

While some interesting works about specifically modelling the diffusion in gliomas are recently starting to appear (Roberts et al., 2017; Zaccagna et al., 2019), this is an environment which is still largely unexplored. Until these novel methodologies gain trust and widely spread recognition, we hope our efforts provided support to the cautious use of existing advanced diffusion techniques to investigate this pathological environment.

Declaration of Competing Interest

The authors declare that they have no known competing financial interests or personal relationships that could have appeared to influence the work reported in this paper.

Appendix A. Supplementary data

Supplementary data to this article can be found online at https://doi.org/10.1016/j.nicl.2022.102968.

References

van Everdingen, K.J., van der Grond, J., Kappelle, L.J., Ramos, L.M.P., Mali, W.P.T.M., 1998. Diffusion-weighted magnetic resonance imaging in acute stroke. Stroke. 29 (9), 1783–1790.

Basser, P.J., Mattiello, J., LeBihan, D., 1994. MR diffusion tensor spectroscopy and imaging. Biophys J. 66 (1), 259–267. https://doi.org/10.1016/S0006-3495(94) 80775-1.

Tournier, J.-D., Mori, S., Leemans, A., 2011. Diffusion tensor imaging and beyond. Magn Reson Med. 65 (6), 1532–1556. https://doi.org/10.1002/mrm.22924.

Alexander, D.C., Dyrby, T.B., Nilsson, M., Zhang, H., 2019. Imaging brain microstructure with diffusion MRI: Practicality and applications. NMR Biomed. 32 (4) https://doi.org/10.1002/nbm.3841.

Wen, Q., Kelley, D.A.C., Banerjee, S., et al., 2015. Clinically feasible NODDI characterization of glioma using multiband EPI at 7 T. NeuroImage Clin. https://doi.org/10.1016/j.nicl.2015.08.017.

Zhang, H., Schneider, T., Wheeler-Kingshott, C.A., Alexander, D.C., 2012. NODDI: Practical in vivo neurite orientation dispersion and density imaging of the human brain. Neuroimage. 61 (4), 1000–1016. https://doi.org/10.1016/j.neuroimage.2012.03.072.

Masjoodi, S., Hashemi, H., Oghabian, M.A., Sharifi, G., 2018. Differentiation of edematous, tumoral and normal areas of brain using diffusion tensor and neurite orientation dispersion and density imaging. J Biomed Phys Eng. https://doi.org/10.31661/jbpe.v0i0.874.

Maximov, I.I., Tonoyan, A.S., Pronin, I.N., 2017. Differentiation of glioma malignancy grade using diffusion MRI. Phys Medica. 40, 24–32. https://doi.org/10.1016/j.ejmp.2017.07.002.

Li, S.-H., Jiang, R.-F., Zhang, J.u.n, Su, C.-L., Chen, X.-W., Zhang, J.-X., Jiang, J.-J., Zhu, W.-Z., 2019. Application of neurite orientation dispersion and density imaging in assessing glioma grades and cellular proliferation. World Neurosurg. 131, e247–e254. https://doi.org/10.1016/j.wneu.2019.07.121.

Kadota, Y., Hirai, T., Azuma, M., Hattori, Y., Khant, Z.A., Hori, M., Saito, K., Yokogami, K., Takeshima, H., 2020. Differentiation between glioblastoma and solitary brain metastasis using neurite orientation dispersion and density imaging. J Neuroradiol. 47 (3), 197–202. https://doi.org/10.1016/j.neurad.2018.10.005.

Caverzasi, E., Papinutto, N., Castellano, A., Zhu, A.H., Scifo, P., Riva, M., Bello, L., Falini, A., Bharatha, A., Henry, R.G., 2016. Neurite Orientation Dispersion and Density Imaging Color Maps to Characterize Brain Diffusion in Neurologic Disorders. J Neuroimaging. 26 (5), 494–498. https://doi.org/10.1111/jon.12359.

Ravi, D., Ghavami, N., Alexander, D.C., Ianus, A., 2019. Current Applications and Future Promises of Machine Learning in Diffusion MRI. In: Mathematics and Visualization. https://doi.org/10.1007/978-3-030-05831-9_9.

van Timmeren, J.E., Cester, D., Tanadini-Lang, S., Alkadhi, H., Baessler, B., 2020. Radiomics in medical imaging—"how-to" guide and critical reflection. Insights Imaging. 11 (1) https://doi.org/10.1186/s13244-020-00887-2.

Aerts, H.J.W.L., Velazquez, E.R., Leijenaar, R.T.H., Parmar, C., Grossmann, P., Carvalho, S., Bussink, J., Monshouwer, R., Haibe-Kains, B., Rietveld, D., Hoebers, F., Rietbergen, M.M., Leemans, C.R., Dekker, A., Quackenbush, J., Gillies, R.J., Lambin, P., 2014. Decoding tumour phenotype by noninvasive imaging using a quantitative radiomics approach. Nat Commun. 5 (1) https://doi.org/10.1038/ncomms5006.

Kaden, E., Kruggel, F., Alexander, D.C., 2016. Quantitative mapping of the per-axon diffusion coefficients in brain white matter. Magn Reson Med. 75 (4), 1752–1763. https://doi.org/10.1002/mrm.25734.

Kaden, E., Kelm, N.D., Carson, R.P., Does, M.D., Alexander, D.C., 2016. Multi-compartment microscopic diffusion imaging. Neuroimage. 139, 346–359. https://doi.org/10.1016/j.neuroimage.2016.06.002.

Daducci, A., Canales-Rodríguez, E.J., Zhang, H., Dyrby, T.B., Alexander, D.C., Thiran, J.-P., 2015. Accelerated microstructure imaging via convex optimization (AMICO) from diffusion MRI data. NeuroImage 105, 32–44.

Steven, A.J., Zhuo, J., Melhem, E.R., 2014. Diffusion kurtosis imaging: An emerging technique for evaluating the microstructural environment of the brain. Am J Roentgenol. 202 (1), W26–W33. https://doi.org/10.2214/AJR.13.11365.

Novikov, D.S., Kiselev, V.G., Jespersen, S.N., 2018. On modeling. Magn Reson Med. 79 (6), 3172–3193. https://doi.org/10.1002/mrm.27101.

Callaghan, P.T., Jolley, K.W., Lelievre, J., 1979. Diffusion of water in the endosperm tissue of wheat grains as studied by pulsed field gradient nuclear magnetic resonance. J. Biophys. 28 (1), 133–141.

Kroenke, C.D., Ackerman, J.J.H., Yablonskiy, D.A., 2004. On the nature of the NAA diffusion attenuated MR signal in the central nervous system. Magn Reson Med. 52 (5), 1052–1059.

Stanisz, G.J., Wright, G.A., Henkelman, R.M., Szafer, A., 1997. An analytical model of restricted diffusion in bovine optic nerve. Magn Reson Med. 37 (1), 103–111. https://doi.org/10.1002/mrm.1910370115.

Veraart, J., Sijbers, J., Sunaert, S., Leemans, A., Jeurissen, B., 2013. Weighted linear least squares estimation of diffusion MRI parameters: Strengths, limitations, and pitfalls. Neuroimage. 81, 335–346. https://doi.org/10.1016/j.neuroimage.2013.05.028.

Gudbjartsson, HáKon, Patz, S., 1995. The Rician distribution of noisy MRI data. Magnetic resonance in medicine 34 (6), 910–914.

Kappy, M.S., 2013. An Introduction to the. Bootstrap. 60 (1), xix–xx. https://doi.org/10.1016/j.yapd.2013.04.017.

Alexander, D.C., 2008. A general framework for experiment design in diffusion MRI and its application in measuring direct tissue-microstructure features. Magn Reson Med. 60 (2), 439–448. https://doi.org/10.1002/mrm.21646.

Frank, P.M., Eslami, M., 1980. Introduction to System Sensitivity Theory. IEEE Trans Syst Man Cybern. 10 (6), 337–338.

Thomaseth, K., Cobelli, C., 1999. Generalized Sensitivity Functions in Physiological System Identification. Ann Biomed Eng. 27 (5), 607–616. https://doi.org/10.1114/1.207.

Bastiani, M., Cottaar, M., Fitzgibbon, S.P., Suri, S., Alfaro-Almagro, F., Sotiropoulos, S.N., Jbabdi, S., Andersson, J.L.R., 2019. Automated quality control for within and between studies diffusion MRI data using a non-parametric framework for movement and distortion correction. Neuroimage. 184, 801–812. https://doi.org/10.1016/j.neuroimage.2018.09.073.

MRtrix3: Advanced tools for the analysis of diffusion MRI data. http://www.mrtrix.org/.

Veraart, J., Novikov, D.S., Christiaens, D., Ades-aron, B., Sijbers, J., Fieremans, E., 2016. Denoising of diffusion MRI using random matrix theory. Neuroimage. 142, 394–406. https://doi.org/10.1016/j.neuroimage.2016.08.016.

Andersson, J.L.R., Skare, S., Ashburner, J., 2003. How to correct susceptibility distortions in spin-echo echo-planar images: Application to diffusion tensor imaging. Neuroimage. 20 (2), 870–888. https://doi.org/10.1016/S1053-8119(03)00336-7.

Andersson, J.L.R., Sotiropoulos, S.N., 2016. An integrated approach to correction for off-resonance effects and subject movement in diffusion MR imaging. Neuroimage. 125, 1063–1078. https://doi.org/10.1016/j.neuroimage.2015.10.019.

Avants, B.B., Tustison, N.J., Song, G., Cook, P.A., Klein, A., Gee, J.C., 2011. A reproducible evaluation of ANTs similarity metric performance in brain image registration. Neuroimage 54 (3), 2033–2044.

Ashburner, John, et al. "SPM12 manual." Wellcome Trust Centre for Neuroimaging, London, UK (2014): 2464.

Panagiotaki, E., Chan, R.W., Dikaios, N., Ahmed, H.U., O'Callaghan, J., Freeman, A., Atkinson, D., Punwani, S., Hawkes, D.J., Alexander, D.C., 2015. Microstructural characterization of normal and malignant human prostate tissue with vascular, extracellular, and restricted diffusion for cytometry in tumours magnetic resonance imaging. Invest Radiol. 50 (4), 218–227. https://doi.org/10.1097/RLI.0000000000000115.

Panagiotaki, E., Walker-Samuel, S., Siow, B., Johnson, S.P., Rajkumar, V., Pedley, R.B., Lythgoe, M.F., Alexander, D.C., 2014. Noninvasive quantification of solid tumor microstructure using VERDICT MRI. Cancer Res. 74 (7), 1902–1912. https://doi.org/10.1158/0008-5472.CAN-13-2511.

Le Bihan, D., Breton, E., Lallemand, D., Grenier, P., Cabanis, E., Laval-Jeantet, M., 1986. MR imaging of intravoxel incoherent motions: Application to diffusion and perfusion in neurologic disorders. Radiology. 161 (2), 401–407. https://doi.org/10.1148/radiology.161.2.3763909.

Nilsson, M., Englund, E., Szczepankiewicz, F., van Westen, D., Sundgren, P.C., 2018. Imaging brain tumour microstructure. Neuroimage. 182, 232–250. https://doi.org/10.1016/j.neuroimage.2018.04.075.

Jelescu, I.O., Veraart, J., Fieremans, E., Novikov, D.S., 2016. Degeneracy in model parameter estimation for multi-compartmental diffusion in neuronal tissue. NMR Biomed. 29 (1), 33–47. https://doi.org/10.1002/nbm.3450.

Novikov, D.S., Fieremans, E., Jespersen, S.N., Kiselev, V.G., 2019. Quantifying brain microstructure with diffusion MRI: Theory and parameter estimation. NMR Biomed. 32 (4) https://doi.org/10.1002/nbm.3998.

Szczepankiewicz, F., Sjölund, J., Ståhlberg, F., Lätt, J., Nilsson, M., Chen, X.i., 2019. Tensor-valued diffusion encoding for diffusional variance decomposition (DIVIDE): Technical feasibility in clinical MRI systems. PLoS One. 14 (3), e0214238. https://doi.org/10.1371/journal.pone.0214238.

Roberts, T.A., Hyare, H., Agliardi, G., et al., 2017. Quantitation of brain tumour microstructure response to Temozolomide therapy using non-invasive VERDICT MRI. bioRxiv. https://doi.org/10.1101/182675.

Zaccagna, F., Riemer, F., Priest, A.N., McLean, M.A., Allinson, K., Grist, J.T., Dragos, C., Matys, T., Gillard, J.H., Watts, C., Price, S.J., Graves, M.J., Gallagher, F.A., 2019. Non-invasive assessment of glioma microstructure using VERDICT MRI: correlation with histology. Eur Radiol. 29 (10), 5559–5566. https://doi.org/10.1007/s00330-019-6011-8.